

Impacts of irrigation expansion on moist-heat stress based on IRRMIP results

Received: 19 August 2024

Accepted: 16 January 2025

Published online: 26 January 2025

 Check for updates

Yi Yao¹✉, Agnès Ducharne², Benjamin I. Cook³, Steven J. De Hertog^{1,4}, Kjetil Schanke Aas⁵, Pedro F. Arboleda-Obando², Jonathan Buzan^{6,7}, Jeanne Colin⁸, Maya Costantini⁸, Bertrand Decharme⁸, David M. Lawrence⁹, Peter Lawrence⁹, L. Ruby Leung¹⁰, Min-Hui Lo¹¹, Narayanappa Devaraju¹², William R. Wieder⁹, Ren-Jie Wu¹¹, Tian Zhou¹⁰, Jonas Jägermeyr^{13,14,15}, Sonali McDermid³, Yadu Pokhrel¹⁶, Maxwell Elling¹⁴, Naota Hanasaki¹⁷, Paul Muñoz¹, Larissa S. Nazarenko³, Kedar Otta¹⁷, Yusuke Satoh¹⁸, Tokuta Yokohata¹⁷, Lei Jin¹⁹, Xuhui Wang¹⁹, Vimal Mishra^{20,21}, Subimal Ghosh²² & Wim Thiery¹

Irrigation rapidly expanded during the 20th century, affecting climate via water, energy, and biogeochemical changes. Previous assessments of these effects predominantly relied on a single Earth System Model, and therefore suffered from structural model uncertainties. Here we quantify the impacts of historical irrigation expansion on climate by analysing simulation results from six Earth system models participating in the Irrigation Model Intercomparison Project (IRRMIP). Results show that irrigation expansion causes a rapid increase in irrigation water withdrawal, which leads to less frequent 2-meter air temperature heat extremes across heavily irrigated areas (≥ 4 times less likely). However, due to the irrigation-induced increase in air humidity, the cooling effect of irrigation expansion on moist-heat stress is less pronounced or even reversed, depending on the heat stress metric. In summary, this study indicates that irrigation deployment is not an efficient adaptation measure to escalating human heat stress under climate change, calling for carefully dealing with the increased exposure of local people to moist-heat stress.

Irrigation increases crop yield and currently accounts for more than 70% of total human freshwater use¹. Irrigation-related water withdrawal and application have substantial impacts on global and regional water, energy, and biogeochemical cycles^{2–5}, and therefore can change the magnitude and pattern of some meteorological conditions^{6–8}. Notably, irrigation has a cooling effect on near-surface temperature^{9,10}, especially during hot extremes^{11,12}. For that reason, irrigation has been proposed as a potential land management strategy for balancing extreme heat escalation under anthropogenic climate change^{12–14}.

Most previous studies only focused on temperature differences, ignoring that human comfort is also affected by heat dissipation¹⁵. Evaporative cooling is one of the main ways humans lose heat¹⁶, and air

humidity and wind speed greatly influence evaporation efficiency¹⁷. These metrics can also be altered by irrigation^{18,19}, suggesting that irrigation-induced impacts on human comfort during heat stress may be complex. Multiple moist-heat metrics were developed to quantify the compound effects of different meteorological conditions on heat stress^{20,21}, and some of them have been used in irrigation-related studies. For example, over intensely irrigated regions in India, the wet-bulb temperature (T_w) was simulated to increase due to irrigation, despite a lowering of the temperature^{22,23}. In addition to the ignorance of changes in air humidity, existing modelling studies generally use a static irrigated land map and rely on a single Earth System Model (ESM), which can introduce uncertainties in their results.

A full list of affiliations appears at the end of the paper. ✉ e-mail: yi.yao@vub.be

To address these limitations, we launched the Irrigation Model Intercomparison Project (IRRMIP) to comprehensively explore the impacts of irrigation expansion on climate and water resources during the 20th century. The IRRMIP protocol consists of two transient AMIP-style²⁴ historical climate experiments, one with and one without irrigation expansion, during the period 1901–2014. Here we analyse IRRMIP simulations from six ESMs to study the impacts of irrigation expansion on historical (moist-)heat stress. We calculate several moist-heat metrics based on 3-hourly 2-m air temperature (T_{2m}), 2-m air relative humidity, and 10-m wind speed. By comparing the results from different experiments and periods, we separate the effects of irrigation expansion and other forcings on high percentiles of these metrics. We aim at consolidating the understanding of irrigation-induced impacts on (moist-)heat stress, facilitating the inclusion of these impacts in future local land-use and land-management planning.

Results

Irrigation expansion drives the increase in water withdrawal

Global area equipped for irrigation has experienced substantial expansion from 1901 to 2014, increasing almost sixfold from $0.5 \times 10^6 \text{ km}^2$ to around $3 \times 10^6 \text{ km}^2$ (Fig. 1a). Expansion mainly happened in some irrigation hot spots, including South Asia (SAS), East Asia (EAS), and Central North America (CNA) (Fig. 2a). In 1901, most of the global irrigated land was concentrated over the regions where rice is the main staple food, such as India, China, and Japan (Fig. S3a). Since 1901, irrigated land has risen slowly over many regions until the 1950s, followed by an accelerated increase during the second half of the century (Fig. 1a). Until 2014, the irrigated areas in India and China experienced intensification and expansion, with some grid cells having a $\geq 40\%$ (of the grid cell area) increase in irrigated area (Fig. 2a, b). Over North America, some new densely irrigated grid cells appear in CNA, while for other regions, the expansion is limited (mostly below 10% of the grid cell area).

The spatial pattern of simulated irrigation water withdrawal (IWW) is in agreement with the distribution of the area equipped for irrigation (Fig. 2c, d). India is still the most intensively irrigated region, consisting of many grid cells ($0.9^\circ \times 1.25^\circ$) with more than 250 mm yr^{-1}

of IWW. The six IRRMIP models simulate a broad range of global IWW ($900\text{--}4000 \text{ km}^3 \text{ yr}^{-1}$ after the year 2000), but the temporal trend of simulations with transient irrigation extent (hereafter referred to as *tranirr*) generally aligns with that of the area equipped for irrigation. Consistent with a previous review⁵, simulated annual IWW during the post-2000 period ranges from ~ 900 to $\sim 4000 \text{ km}^3 \text{ yr}^{-1}$ (Fig. 1c–h), due to different representations of irrigation in these models. CESM2, CESM2_gw, and NorESM2 show high similarity because they share the same atmosphere and land models, with comparably small differences in specific sub-models (see Supplementary Note 1).

Based on IWW and irrigated area, we select several regions, including West North America (WNA), CNA, North Central America (NCA), Mediterranean (MED), West Central Asia (WCA), SAS, EAS, and Southeast Asia (SEA) (Fig. 2a), to calculate regional irrigation water quantities (Fig. 1c–h). SAS is the region with the highest IWW in all models, but its relative importance varies. For example, after the year 2000, SAS accounts for around one-third of global IWW simulated by CESM2 (32.4–35.8%), CESM2_gw (31.4–35.1%), E3SM (27.5–41.8%), and NorESM (32.8–35.1%), but in IPSL-CM6, this fraction is less than one-fourth (16.0–20.4%). WCA consumes the second-highest quantity of IWW, even though its area equipped for irrigation is less than EAS. This indicates that simulated IWW is dependent not only on the area equipped for irrigation but also on other factors, such as background climate conditions.

Different feedback from heat and moist-heat stress to irrigation expansion

Here we focus on T_{2m} , HUMIDEX (HU; Eq. (2)), and T_w (Eq. (4)) warm extremes, as many other metrics are weighted average values of T_{2m} and T_w . Changes in high percentiles of these three metrics could be interpreted as the impacts of irrigation expansion and other forcings on dry heat stress (T_{2m}), human comfort (HU), and humid heat stress (T_w) (Table 1). In the *tranirr* experiment, climate change, land use change, and irrigation expansion, are all transient throughout the simulation period, and in the *1901irr* experiment, the only difference is that irrigation extent is fixed at the level in year 1901 (simulation protocol of IRRMIP can be found in Supplementary Note 2).

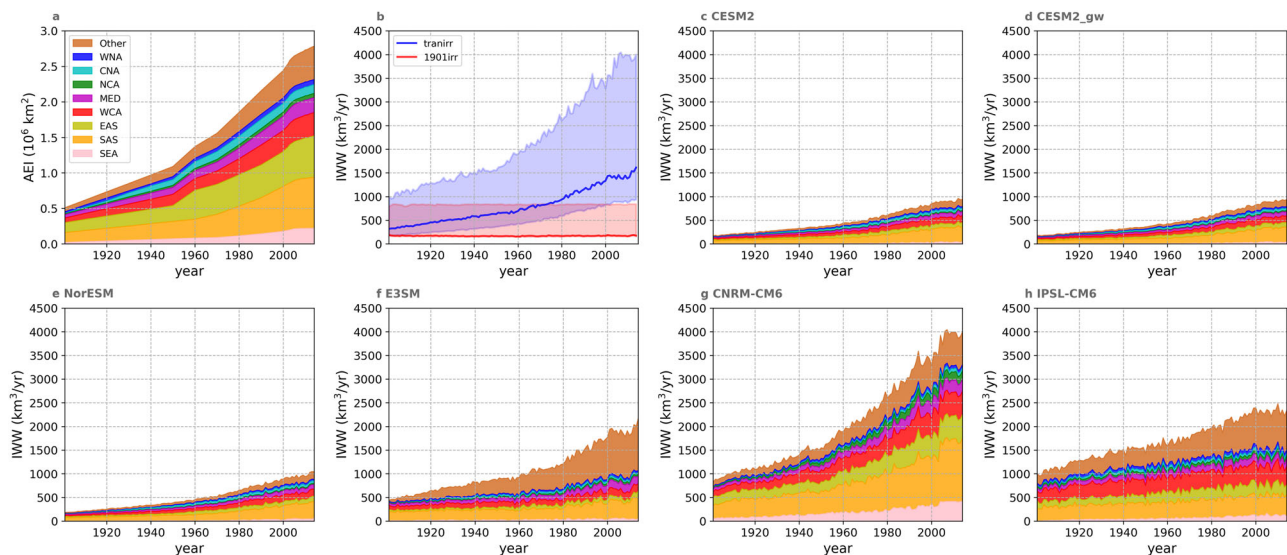


Fig. 1 | Historical increase in area equipped for irrigation and simulated irrigation water withdrawal. a Global and regional time series of area equipped for irrigation (AEI) in 1901–2014. The area equipped for irrigation data is from the Land-Use Harmonization phase 2 (LUH2) project⁵⁷, and the grid cells corresponding to IPCC reference regions are indicated in Fig. 2a. **b** Simulated mean global irrigation water withdrawal (IWW) with (blue: *tranirr*) by all six models and without (red: *1901irr*) irrigation expansion by five models (except IPSL-CM6). The line indicates

the median value of six (or five) models and the range indicates the maximum and minimum values. Note that IWW of CNRM-CM6-1 is applied as an external input, which is the irrigation fluxes from a global reconstructed hydrological dataset based on simulations³⁴, and for the *1901irr* experiment of IPSL-CM6, irrigation is switched off. **c–h** Global and regional IWW (*tranirr*) simulated by CESM2 (c), CESM2_gw (d), NorESM (e), E3SM (f), CNRM-CM6-1 (g), and IPSL-CM6 (h).

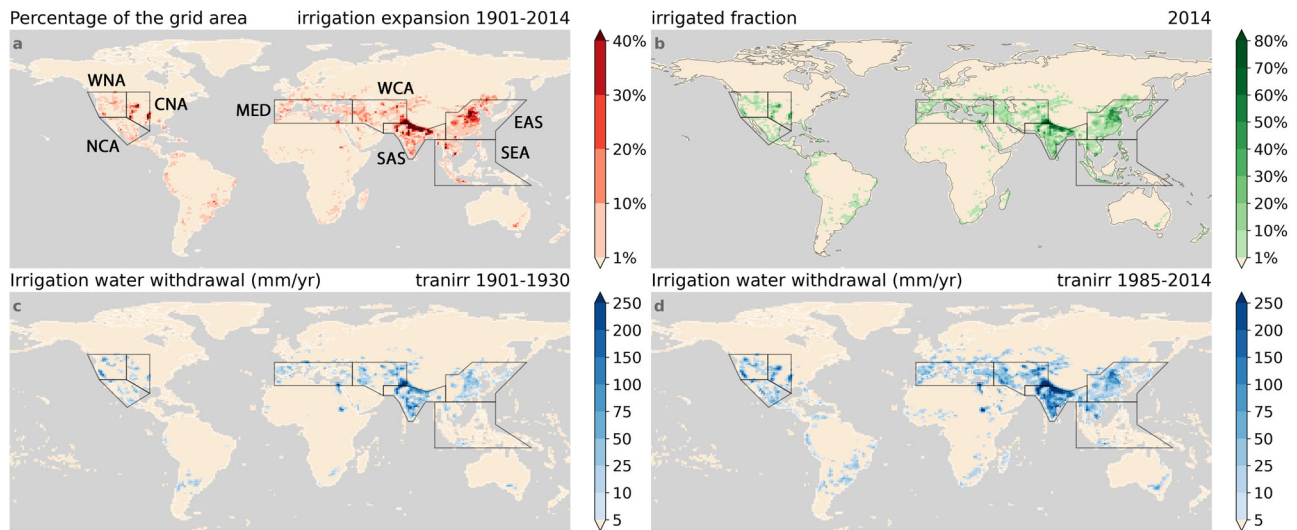


Fig. 2 | Spatial pattern of irrigation expansion and simulated irrigation water withdrawal in different periods. **a** Increase in irrigated fraction between 1901 and 2014, and the IPCC reference regions⁷¹ used in the analysis. **b** Irrigated fraction in the year 2014 (Irrigated fraction in the year 1901, 1941, and 1981 could be found in Fig. S3a–c). The grid resolution is the simulation resolution of CESM2, CESM2_gw, and NorESM ($0.9^\circ \times 1.25^\circ$). **c, d** Multi-model mean simulated annual irrigation water

withdrawal (IWW) with transient irrigation extent (*tranirr*) during the first 30 years (1901–1930: **c**) and the last 30 years (1985–2014: **d**). The figure showing results from all individual models can be found in Fig. S15. Multi-model mean simulated annual IWW with fixed irrigation extent (*190Iirr*) during the two periods can be found in Fig. S3e, f.

Table 1 | Approach to separate the impacts of different forcings

Reference exp_period	New exp_period	Forcings
190Iirr(1901–1930)	tranirr(1985–2014)	all forcings (greenhouse gas emissions, land use change, irrigation expansion, etc.)
190Iirr(1901–1930)	190Iirr(1985–2014)	all forcings except irrigation expansion
190Iirr(1985–2014)	tranirr(1985–2014)	irrigation expansion

By comparing the last-30-year of *tranirr* (*tranirr(1985–2014)*) to the first-30-year of *190Iirr* (*190Iirr(1901–1930)*), we can quantify the impacts of all forcings (greenhouse gas emissions, land use and land management change, irrigation expansion, etc.). Similarly, the difference between the first- and the last-30-year periods of *190Iirr* (*190Iirr(1901–1930)* and *190Iirr(1985–2014)*) gives the impacts of all forcings minus irrigation expansion. Finally, by subtracting the outputs of *tranirr(1985–2014)* from *190Iirr(1985–2014)*, we obtain the impacts of irrigation expansion.

We first calculate the 99.9th percentile values (one-in-1000 time steps warm event) of three metrics in three exp_periods (*190Iirr(1901–1930)*, *190Iirr(1985–2014)* and *tranirr(1985–2014)*), and take the one of *190Iirr(1901–1930)* as the reference (Fig. 3a–c). Several irrigation hot spots, like SAS, WCA, NCA, and CNA, are also extreme heat hot spots, with a 99.9th percentile value of T_{2m} exceeding 40°C in many grid cells. Other forcings cause a general warming signal ($+0.5$ to $+2^\circ\text{C}$, see Fig. 3g), except in some areas over SAS and EAS, which may be attributed to the increasing aerosol concentrations^{25,26}. Irrigation expansion has substantial cooling impacts in heavily irrigated grid cells ($>1^\circ\text{C}$) and weaker impacts over surrounding grid cells ($<0.5^\circ\text{C}$) (Fig. 3j). This cooling effect creates regional irrigation-induced ‘cooling islands’ against the global warming background, like the Indo-Gangetic Plain and several grid cells in Central USA (Fig. 3d). Irrigation expansion’s cooling impacts on the extreme value of HU are much less substantial in magnitudes (Fig. 3k), as a result of the increased humidity, and the ‘cooling islands’ do not exist if HU is picked as the indicator (Fig. 3e). Interestingly, T_w extreme value is only affected by irrigation expansion in limited regions, like several pixels in WCA, CNA, and the Mediterranean, but over other traditional hot spot regions like SAS and EAS, the impacts are negligible (Fig. 3l).

To quantify the changes in extreme heat events frequency, we then calculate the probability ratio (PR: Eq. (5) and Table 1) of T_{2m} , HU, and T_w warm extremes between different exp_periods (Fig. 4, S4–6). We find that the pattern of these impacts is similar to those on the absolute value of heat extreme events (Fig. 3). Other forcings, especially greenhouse gas emissions, contribute to a warmer world, with >4 times increased frequency for the events of all three metrics in most grid cells in tropical and sub-tropical regions (Figs. S4f, S5f, and S6f). Most models agree that irrigation expansion substantially reduces the frequency of T_{2m} extremes, especially in SAS, WCA, and CNA (Fig. 4a, d, g and S4i). However, its impacts on HU and T_w are much less pronounced and are also less consistent among models (Fig. 4b, c, e, f, h, i, S5i and S6i). Similarly, for T_w , the dampening impacts of irrigation on extreme high events disappear over the most intensely irrigated area like India and are reversed to an intensifying effect in the Central CNA and WCA, where the 99.9th percentile T_w event happens ≥ 2 times more often due to irrigation expansion (Fig. 4c, f).

The more extreme the T_{2m} heat events are, the more pronounced irrigation expansion-induced impacts become (Fig. S4). The impacts of irrigation expansion on T_{2m} are mainly limited to irrigation hot spots for the 99th percentile heat event, e.g., large changes in PR (that is, >2 times less likely) are only found in North India and Central USA (Fig. S4g). When the events get more extreme (99.5th percentile and 99.9th percentile), the affected areas expand around these hot spots and also appear in other regions like Europe and East China (Fig. S4h, i). The slight cooling impacts on HU are also more pronounced when events get more extreme (Fig. S5), and the warming effects on T_w do not change substantially (Fig. S6). We also calculate irrigation expansion’s impacts on other moist-heat metrics (Fig. S7, description of metrics can be found in Supplementary Note 3). We find that the

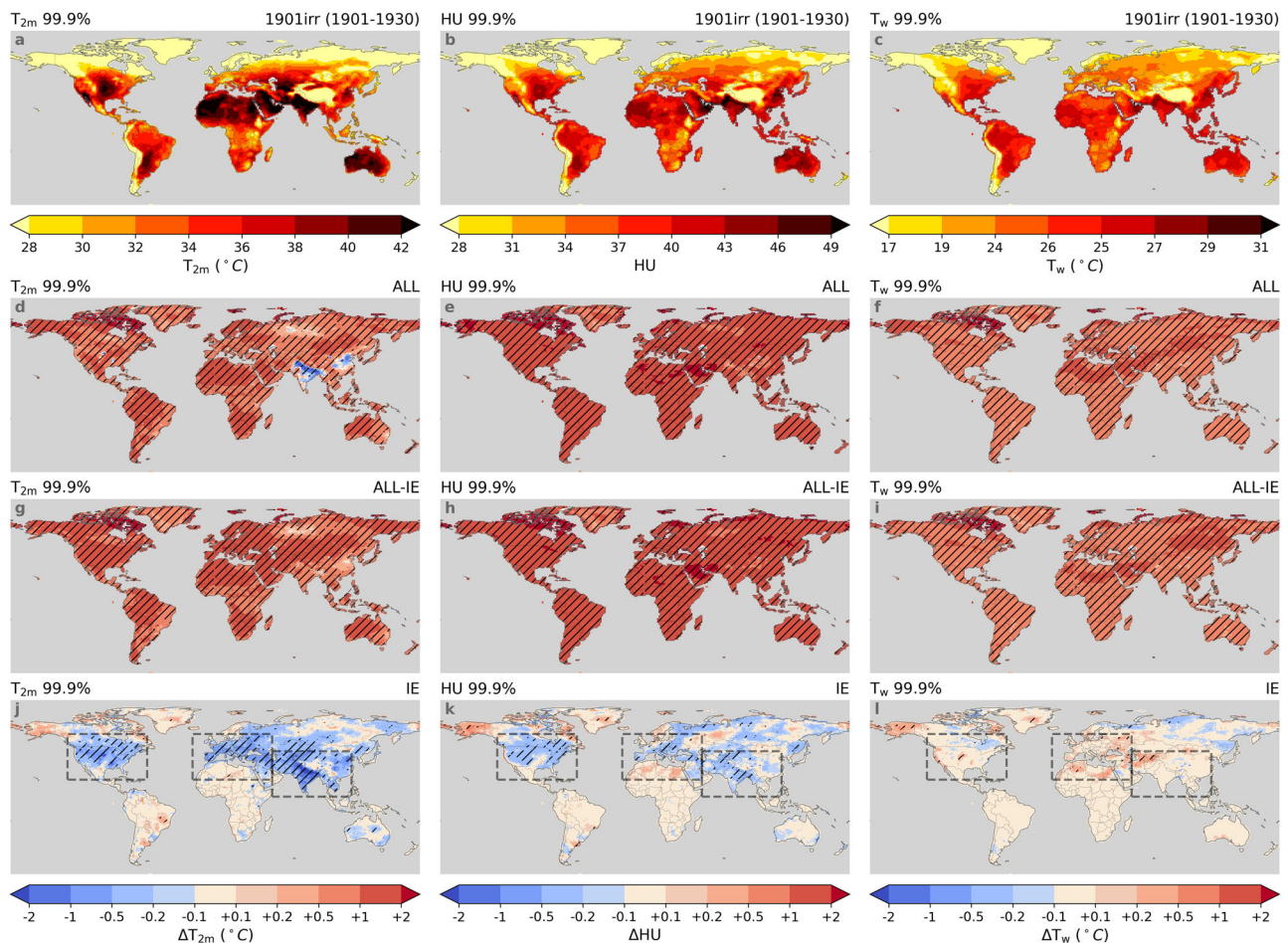


Fig. 3 | Heat and moist-heat extremes and impacts of different forcings on them. **a–c** Multi-model mean absolute values of the 99.9th percentile values of 2-m air temperature (T_{2m} ; **a**), HUMIDEX (HU; **b**), and wet-bulb temperature (T_w ; **c**) of the first 30 years (1901–1930) in the simulations without irrigation expansion (*I90Iirr*). **d–f** Multi-model mean impacts of all forcings (ALL: greenhouse gas emissions, land use and land management change, irrigation expansion, etc.) (**d–f**), all forcings except irrigation expansion (ALL-IE: **g–i**), and irrigation expansion (IE:

j–l) on the 99.9th percentile values of T_{2m} (**d, g, j**), HU (**e, h, k**), and T_w (**f, i, l**). Impacts are calculated by subtracting the values in the new exp_period by those in the reference exp_period (see Table 1). Hatches indicate that signals (>0.1 or <-0.1) are agreed by ≥ 5 of 6 models (results for the individual models are presented in Supplementary Fig. S16–21). Results for other extreme event percentiles (the 99th and 99.5th) are shown in Supplementary Figs. S28–36.

significance of irrigation expansion's impacts on the apparent temperature is similar to HU, and as for other moist-heat metrics, the magnitude and consistency depend on the weight of T_w and T_{2m} .

We calculate the average annual hours (weighted by areas) exposed to extreme events of the grid cells with more than 40% (of the grid area) irrigation expansion (Fig. 5). The average annual hours exposed to T_{2m} extreme events show a slight increase in the first half of the century, then increases rapidly between 1950 and 1980, and keeps steady in the last decades. Irrigation expansion causes a decreasing trend in the hours exposed to heat extremes in heavily irrigated regions, in spite of global warming. However, for HU, the cooling impacts of irrigation expansion are quite small, thus the hours exposed to extreme HU events still increase, but at a slightly slower speed than those without irrigation expansion. Interestingly, the hours exposed to T_w extreme events for both *I90Iirr* and *tranirr* remain almost unchanged until 1980. After 1980, this starts to rise rapidly. In the case of *tranirr*, the hours are slightly higher than *I90Iirr*, indicating the intensifying impact of irrigation expansion over these grid cells. Since T_{2m} extremes are the most substantially affected events, we also calculate the average annual hours exposed to different magnitude of T_{2m} extreme events (the 99.0th, the 99.5th and the 99.9th percentile events) over different groups of grid cells (with 0–20%, 20–30%,

30–40%, and more than 40% of irrigation expansion) (Fig. S8). Despite the difference in magnitudes, irrigation expansion has similar reducing impacts on all degrees of T_{2m} extreme events, which become more substantial with the extent of irrigation expansion.

Irrigation expansion-induced impacts on energy fluxes

T_{2m} generally has positive correlation with the land surface temperature and sensible heat flux (SHF)²⁷, and land surface temperature directly determines the upwelling longwave radiation flux (LW_{up}). Results show that both LW_{up} (Fig. 6a) and SHF (Fig. 6b) decrease due to irrigation expansion, which explains its cooling impacts. Based on surface energy balance, the sum of SHF and LW_{up} could be calculated as Eq. (1):

$$LW_{up} + SHF = SW_{down} - SW_{up} + LW_{down} - LHF - R \quad (1)$$

where SW_{down} and SW_{up} denote the down/upwelling shortwave radiation, LW_{down} is the downwelling longwave radiation, LHF is the latent heat flux, and R means the residual term which includes the heat storage and fluxes in ground, water, vegetation, as well as anthropogenic heat sources and sinks.

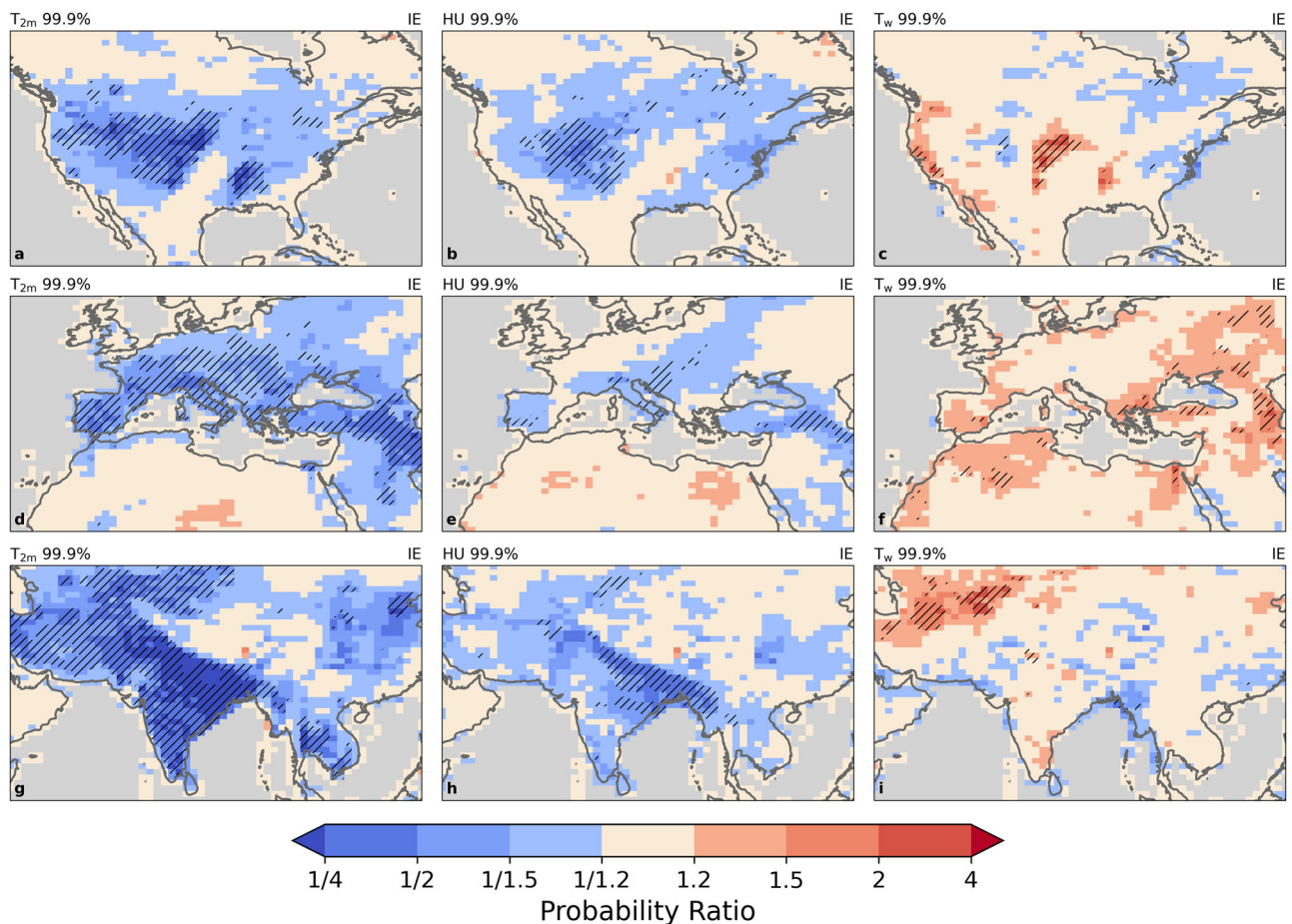


Fig. 4 | Changes in the frequency of (moist)-heat extreme events induced by irrigation expansion. **a–i** Impacts of irrigation expansion (IE) on the frequency of the events in which 2-meter air temperature (T_{2m} : **a, d, g**), HUMIDEX (HU: **b, e, h**), and wet-bulb temperature (T_w : **c, f, i**) exceed their 99.9th percentile values of the first 30 years (1901–1930) in the simulations without irrigation expansion (*190Iirr*) (shown in Fig. 3a–c). The spatial coverage include three regions: 130–60°W and 20–60°N (**a–c**), 20°W–50°E and 20–60°N (**b–f**), 50–120°E and 5–45°N (**g–i**). The location of these regions can be found in Fig. 3j–l. Impacts are quantified by probability ratio (PR: Eq. (5)) which is calculated by dividing the events frequencies

in the new exp_period by those in the reference exp_period (see the lowest row in Table 1), and the values are the sixth root of the product of PR calculated from the outputs of six ESMs. Hatches indicate that signals (>1.2 or $<1/1.2$) are agreed by ≥ 5 of 6 models (results of individual models can be found in Fig. S22–27). Results of other metrics can be found in Fig. S7. In Fig. S4–6, the impacts of all forcings (ALL), all forcings except irrigation expansion (ALL-IE), and IE on the frequency of the events in which T_{2m} , HU, and T_w exceed their 99th, 99.5th, 99.9th percentile values during 1901–1930 in the simulations *190Iirr* are shown (results of other metrics can be found in Supplementary Figs. S37–42).

It is known that irrigation practices substantially increase LHF due to enhanced evapotranspiration^{7,10,28} (Fig. 6c), but its impacts on other radiative fluxes are less pronounced (Fig. 6d–f), which align with previous studies^{10,28,29}. In general, increase in LHF is the main reason for irrigation’s cooling impacts, which, however, also is the origin of negative impacts of higher humidity. Some other measures could be considered to provide additional cooling while avoiding the moistening effects, like enlarging the albedo (increasing SW_{up})¹³, and the most importantly, reducing greenhouse gas concentrations (decreasing LW_{down}). In addition, switching from low-efficiency irrigation to high-efficiency irrigation may also help reducing exposure to moist-heat stress³⁰.

Discussion

Six ESMs simulate a broad range of IWW (-900 to -4000 $\text{km}^3 \text{yr}^{-1}$ after the year 2000) with a median value of around 1500 $\text{km}^3 \text{yr}^{-1}$ (Fig. 1), which is lower than the value of 2761 $\text{km}^3 \text{yr}^{-1}$ reported for the period 2005–2007³¹. Most models, especially those which have CLM5 as their land model, substantially underestimate the global IWW, which could be attributed to its over-conservative irrigation water demand calculation²⁸. A new modification has been made by implementing

different irrigation techniques²⁸, in which the non-effective water consumption is more comprehensively considered, outperforming substantially compared to the original module at global or regional levels. In E3SM a slightly higher IWW is simulated, possibly due to the higher spatial resolution and its added features like surface/groundwater demand separation³², and an interactive surface water withdrawal module³³. The overestimation of CNRM-CM6-1 originates from an external dataset reconstructed with a global hydrological model³⁴, in which the irrigation water abstraction from groundwater is not limited by water resources³⁵. In IPSL-CM6³⁶, a constraint is imposed on IWW based on the water availability, with the parameters sensitivity tests and calibration, showing a superior performance of reproducing global IWW despite the slight underestimation. Overall, the implementation of irrigation techniques, groundwater withdrawal, water resources management, water availability, and the calibration and validation of irrigation-related parameters, should all be considered in the next generation of irrigation representations in ESMs.

Despite the wide range of simulated IWW, ESMs used in this study agree that irrigation has a cooling impact on local hot extremes, which is consistent with previous studies^{10,12,13}. This cooling impact has the potential of mitigating the heat exposure of both local inhabitants and

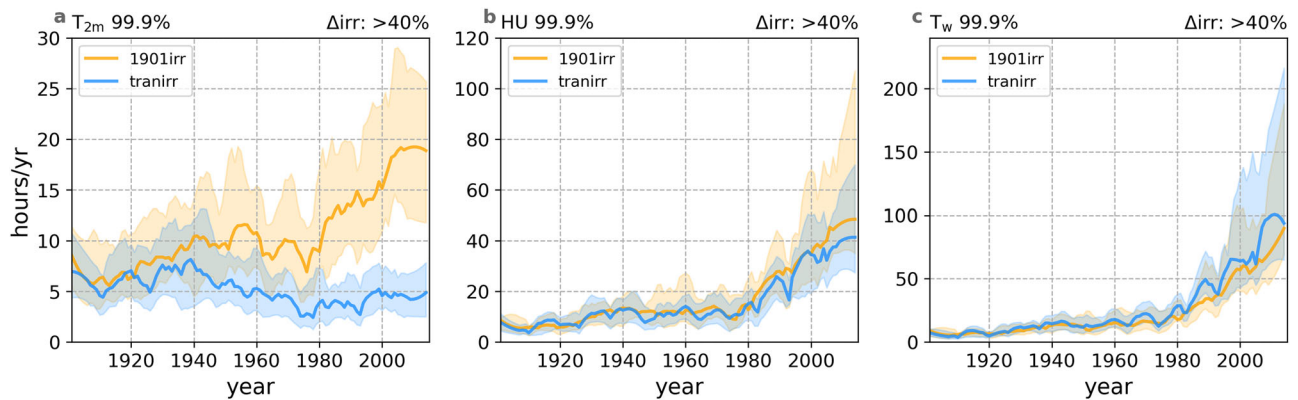


Fig. 5 | Increase in annual hours exposed to (moist-)heat extreme events over the grid cells with the most substantial irrigation expansion. a–c Time series of the annual hours over the grid cells with $\geq 40\%$ of irrigated fraction increase (in the year 2014 compared to the year 1901) of 2-m air temperature (T_{2m} ; **a**), HUMIDEX (HU; **b**), and wet-bulb temperature (T_w ; **c**) warm extremes. The warm extremes are defined as the period when T_{2m} , HU, and T_w exceed their 99.9th percentile values of the first 30 years (1901–1930) in the simulations without irrigation expansion

(1901irrigation). Lines indicate the median value among six models and ranges indicate the middle four of six models. Curves were smoothed using Savitzky-Golay filtering (order = 2, window = 15)⁷². The range of the y-axes are different for three sub-plots. Results of various extreme events of T_{2m} over grid cells with different extent of irrigation expansion is shown in Fig. S8, and similar results of HU and T_w can be found in Figs. S43–44.

crops³⁷. However, reduced temperature does not decrease the frequency of moist-heat stress by a similar magnitude, and most ESMs even believe that historical irrigation expansion has an intensifying impacts on T_w extremes in some regions like the Central USA and West Asia (Fig. 3I), possibly endangering local population. Different from the cooling impacts on temperature extremes, the impacts of irrigation on moist-heat extremes are less substantial. As mentioned above, over two intensely irrigated regions, India and East China, extreme events of T_w do not show pronounced changes in both magnitude and frequency (Figs. 3 and 4) due to irrigation expansion. Two previous studies, a global one using the Goddard Institute for Space Studies (GISS) climate model²³ and a regional one based on Massachusetts Institute of Technology Regional Climate Model³⁸, found that irrigation increases the average values T_w more substantially than the extreme values over the same regions. It implies that the most extreme T_w events may not happen during the heavily irrigated season. Thus, we calculate multi-year mean monthly IWW during the period 1985–2014 of *tranirrigation* experiment (Fig. S9), monthly maximum T_{2m} , HU, and T_w during the same period but of *1901irrigation* experiment (Fig. S10–12), which confirms this hypothesis. In India, high IWW appears in April to June, high T_{2m} extremes exist in May to June, while HU peaks from June to August, and T_w from July to August. This temporal mismatch has also been argued by some researchers^{39,40}, both regarding heat and moist-heat extremes. Irrigation expansion-induced impacts on annual mean, maximum, minimum temperature (Fig. S13) and specific humidity (Fig. S14) also show that T_w is more substantially affected where both annual maximum temperature and specific humidity match temporally the irrigation season, like WCA and CNA. However, if limiting the study period to irrigation season, some studies still found evidence of irrigation-induced warming on T_w extremes in India^{22,41}. Over East China, in contrast, the most intense irrigation season generally overlaps with the peak season for T_{2m} , HU, and T_w , and a previous study has attributed weak impacts of irrigation in this area to a lower intensity of AEI expansion than India and local climatic conditions⁴¹.

Similar to previous ESM-based impact studies regarding moist-heat metrics^{42,43}, we use temperature, moisture, and wind speed at the grid-cell level which are averaged based on values from different land cover tiles. Thus, coarse-resolution simulations' suitability to calculate human heat metrics may be questionable, as sub-grid scale extreme values could be masked. Constrained by computational resources, conducting long-term high-resolution global simulations at less than 100 km resolution is very expensive. In addition, the impacts of

agricultural irrigation on neighbouring non-irrigated areas, especially urban areas with high population density, should be investigated more comprehensively. A previous study highlighted the higher exposure of cities surrounded by irrigated cropland in India to moist-heat stress, as a combined consequence of irrigation and urban heat island effect⁴¹. Unfortunately, urban regions are still poorly resolved in current coarse-resolution ESMs. Despite these limitations, those simulations remain important for understanding the spatial distribution and temporal trend of irrigation-induced impacts on moist-heat stress. Furthermore, previous studies have assessed the suitability of various moist-heat metrics based on their correlation with local mortality datasets, and discovered that the optimal metric varies among countries and cities^{44,45}. The range of moist-heat metrics presented here enables finely tailored investigation of irrigation's impacts on environmental health at local scales. Note that both HU and T_w are designed for human beings, so the results here are not suitable for detecting irrigation-induced impacts on crops and natural plants, which requires better understanding of interactions between plant growth, temperature, and humidity.

In summary, our study stresses an over-optimism regarding irrigation's health benefits, which ignores the impacts of increased air humidity on human comfort. Different metrics extremes have various feedback to irrigation expansion, highlighting the importance of better understand the most suitable metrics for people with different races, genders, ages, health conditions, etc. As a metric commonly used in outdoor activities guidance, T_w extreme events are even intensified by irrigation expansion in some regions. Under global warming scenarios, intolerable T_w events will occur more frequently, especially in South Asia, Central North America, and East Asia⁴⁶. Even more troublesome, the maximum T_w is tied to atmospheric buoyancy, which is determined by global mean surface temperatures^{47,48}. T_w will increase to the new irrigated value, and scale with global mean temperature changes⁴⁶. This calls for better monitoring of local moist-heat metrics to inform exposed communities of the potential danger, and the exploration of potential solutions.

Methods

Participating ESMs and simulation protocol

Six combinations of state-of-art Earth system models (ESMs) and irrigation parametrizations are used in this study: the Community Earth System Model version 2 (CESM2)⁴⁹, CESM2 with groundwater withdrawal and flow representation (CESM2_gw)⁵⁰, the Institut

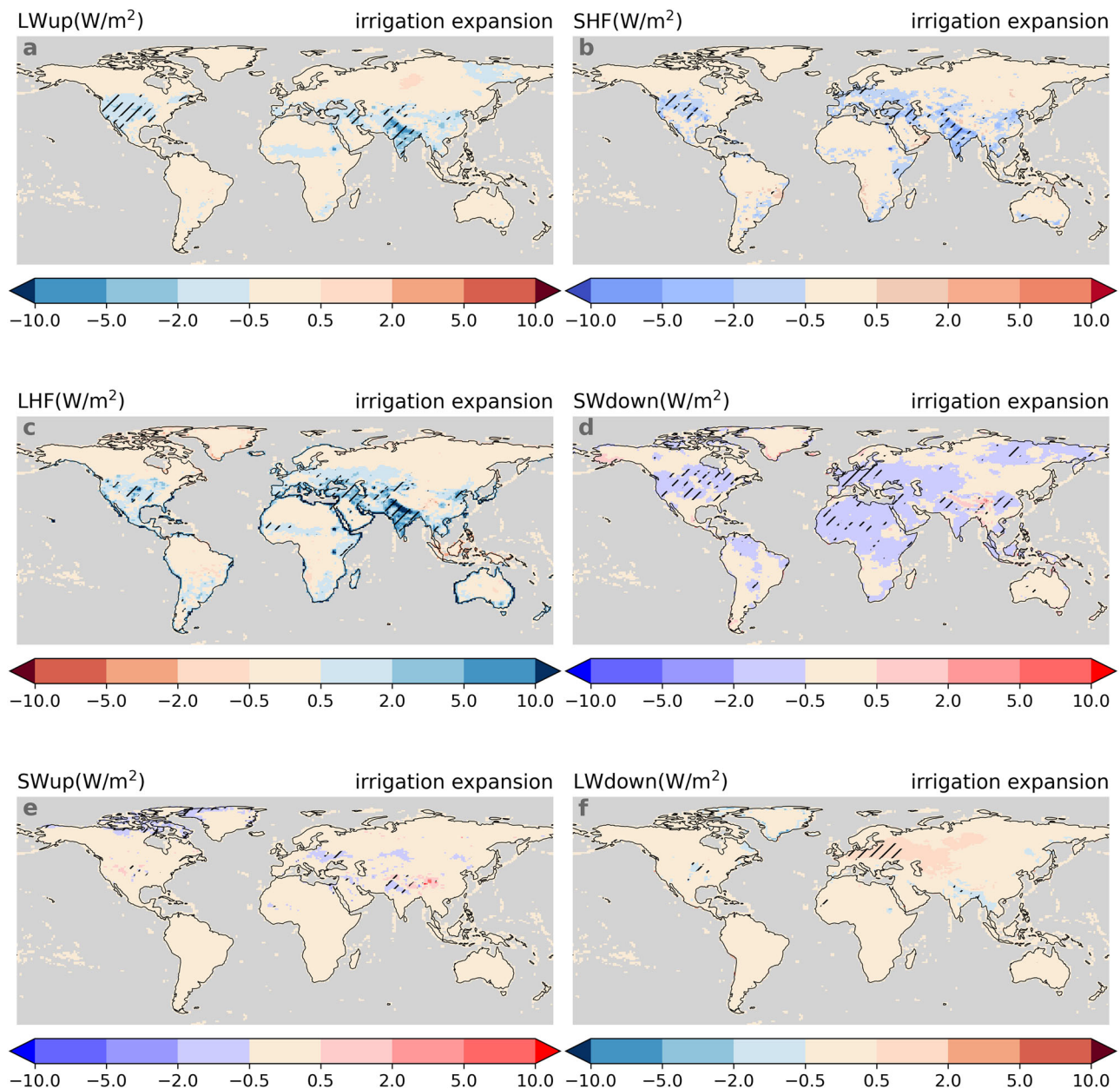


Fig. 6 | Impacts of irrigation expansion on land surface energy fluxes.

a–f Impacts of irrigation expansion on upwelling longwave radiation (LWup: **a**), sensible heat flux (SHF: **b**), latent heat flux (LHF: **c**), downwelling shortwave radiation (SWdown: **d**), upwelling shortwave radiation (LWup: **e**), and downwelling

longwave radiation (LWdown: **f**). Impacts are calculated by subtracting the values in the new exp_period by those in the reference exp_period (see Table 1 row 3). Hatches indicate that signals (>0.5 or <-0.5 W/m²) are agreed by ≥ 5 of 6 models.

Pierre-Simon Laplace Climate Model version 6 (IPSL-CM6)⁵¹ with a newly developed irrigation scheme³⁶, the Norwegian Earth System Model version 2 (NorESM2)⁵², the Energy Exascale Earth System Model Version 2 (E3SMv2)⁵³ with active two-way coupled irrigation scheme³³, and the Centre National de Recherches Météorologiques Climate Model version 6 (CNRM-CM6-1)^{54,55}. Irrigation is represented in different ways in these models, which can be divided into two categories: soil-moisture-based schemes and external forcing applications (only for CNRM-CM6-1). Differences between soil-moisture-based irrigation modules relate to irrigation triggers, start time, duration, amount, and the method of water application. The employed ESMs provide the option to customise irrigation-related parameters, but in this study, all ESMs used default parameter values. CESM2, CESM2_gw, and NorESM2, share identical or similar land system models, which explains

why they show strong consistency between each other. However, their differences in atmospheric models and features in the irrigation scheme, still represent an added value to this study. More detailed description of ESMs and their irrigation representations could be found in Supplementary Note 1.

We design two historical experiments in this study: with (*tranirr*) and without (*1901irr*) historical irrigation expansion. The simulations of both experiments follow the protocol of AMIP simulations in CMIP6 with the same input data⁵⁶, which means that the ocean model is switched off and sea surface temperatures are prescribed. To better capture the signal of irrigation extent increase in the 20th century, we select a simulation period of 1901–2014. The only difference between the two experiments is that in *tranirr*, irrigation extent is transient, while in *1901irr*, the irrigation extent is fixed at the level in the year

1901. One exception is IPSL-CM6, where irrigation is entirely switched off for *I90Iirr*, and we include outputs of this ESM in the analysis as in the year 1901, irrigated fraction is very limited (Fig. S3a). The land-use map and time-series data used in these simulations are from the Land-Use Harmonization phase 2 project (LUH2⁵⁷), in which all crop management activities-related data, including irrigated land distribution, is obtained from the History Database of the Global Environment 3.2 (HYDE 3.2)⁵⁸. The irrigated land data from HYDE 3.2 during the period 1901–2014 has multiple sources: for the period pre-1960, the data is collected directly from the global historical irrigation data set (HID)⁵⁹, and for the post-1960 period, the numbers are calculated by multiplying the term “area equipped for irrigation” in FAO statistics⁶⁰ by the fraction of actual irrigated area in area equipped for irrigation from HID.

Climate extremes

Most models report output variables at the 3-hourly frequency to enable analysis of sub-daily extremes, but CNRM-CM6-1 only provides daily mean, maximum, and minimum values, so we calculate several moist-heat metrics based on daily maximum temperature and minimum air relative humidity to calculate the maximum metrics consistent with a previous study⁶¹, thereby assuming that the lowest relative humidity occurs when the temperature is maximum.

HUMIDEX (HU) is a feel-like heat stress metric developed in the late 1970s, and it was first used for the meteorological service in Canada⁶². It is calculated as Eq. (2):

$$HU = T_c + \frac{5}{9} (e_{RH} - 10) \quad (2)$$

where T_c is the temperature at 2-meter height (°C), e_{RH} (Pa) is the vapour pressure calculated based on relative humidity (RH) and saturated vapour pressure (e_s in Pa), as shown in Eq. (3):

$$e_{RH} = RH e_s, \quad (3)$$

HU is still used by the Canadian Centre for Occupational Health and Safety (CCOHS) to inform the general public if the weather conditions may be comfortable based on the following thresholds: 20–29, 30–39, 40–45, and over 46 represent the warning of ‘little discomfort’, ‘some discomfort’, ‘great discomfort’, and ‘dangerous’, respectively⁶³.

T_w is a measure of heat stress considering the maximum potential evaporative cooling impact⁶⁴. It can be measured by a thermometer covered in water-soaked cloth over which air is passed⁶⁵. The calculation of T_w is very computationally expensive, so we employ a simplified method⁶⁶, as indicated in Eq. (4):

$$T_w = T_c \arctan(0.151977\sqrt{RH + 8.313659}) + \arctan(T_c + RH) - \arctan(RH - 1.676331) + 0.00391838RH^{3/2} \arctan(0.023101RH) - 4.68035 \quad (4)$$

Based on previous studies^{64,67}, when T_w is over 31 °C, physical labour becomes impossible, and exposure to T_w exceeding 35 °C for more than 6 h is dangerous even for healthy individuals. However, the maximum evaporative cooling (swamp cooler) is not easy to approach, as in previous heatwave events, high casualties already existed even if the T_w is less than 28 °C⁶⁸. Other metrics described in Supplementary Note 3 are also calculated based on simulations by all six models, except that we do not calculate the apparent temperature from CNRM-CM6-1 outputs, given the lack of the appropriate wind speed variable.

Data processing

Outputs from E3SM, IPSL-CM6, and CNRM-CM6-1 are firstly regridded to the resolution of CESM2, CESM_gw, and NorESM

($0.9^\circ \times 1.25^\circ$) (original resolution can be found in Supplementary Note 2), and then the moist-heat metrics are calculated (Eqs. (2) and (4)). After calculating the moist-heat metrics, we further processed the results to separate the impacts of irrigation expansion from other forcings. We first calculated irrigation expansion’s impacts on the absolute values of extreme events as well as surface energy fluxes. We select two periods, the first 30 years (1901–1930) and the last 30 years (1985–2014), for both simulations (*tranirr* and *I90Iirr*) to calculate the impacts of all forcings, all forcings except irrigation expansion, and irrigation expansion, on near-surface climate (see Table 1). We assume that the difference between the results during 1901–1930 of *I90Iirr* and those during 1985–2014 of *tranirr* represent the consequence of all forcings. The difference between the results during the two periods for the *I90Iirr* simulations is assumed to be the consequence of other forcings. The difference between these two simulations during the 1985–2014 period is assumed to represent the impacts of irrigation expansion as the only difference between them is whether irrigation extent is transient.

Apart from the absolute value of extreme events, we also calculate the probability ratio (PR) for several extreme events, which has been used in previous studies to show the changes in climate extreme events frequency^{12,69}. The extreme events defined in this study are based on percentile values, e.g., a 99th percentile event means that in the reference period, it happens once per 100 time steps (3 h per 300 h for 3-hourly outputs), or in other words, it indicates the 1% time steps with the most extreme values. Considering that outputs from CNRM-CM6-1 is at a daily frequency, we select the 92nd, 96th, and 99.2nd percentile events for this ESMs to represent the 99th, 99.5th, and 99.9th percentile events simulated by other ESMs. This is based on an assumption that those extreme events calculated based on maximum temperature and minimum humidity last 3 h during the day, so a 92nd percentile value means 8 days per 100 days and then 24 h per 2400 h, which is equal to 3 h per 300 h for 3-hourly outputs. The PR is calculated as:

$$PR = \frac{P_{new}(X_{ext})}{P_{ref}(X_{ext})}, \quad (5)$$

where $P_{new}(X_{ext})$ is the probability of a certain kind of extreme event (X_{ext}) during the new exp_period and $P_{ref}(X_{ext})$ is the probability of the same kind of event during the reference exp_period. Let us assume, for example, that the 99th percentile value of T_{2m} is 33 °C in the reference exp_period, meaning the extreme events are the ones with $T_{2m} > 33$ °C: if the frequency of these events is 4% in the new exp_period, then the PR is 4. Thus, a PR of more than 1 indicates that this event occurs more frequently in the new exp_period compared to the reference exp_period, and vice versa. Similar to absolute values, we also select two periods (1901–1930 and 1985–2014) for both *tranirr* and *I90Iirr*, then calculate the PR between them for the 99.0th, 99.5th, and 99.9th percentile events for T_{2m} , HU, and T_w . To further investigate the temporal trend of irrigation expansion’s impacts, we calculated the mean value of annual hours exposed to warm extremes for four groups of grid cells, with irrigation expansion of 0–20%, 20–30%, 30–40%, and more than 40%.

Data availability

Data generated in this manuscript have been deposited in the figshare database with the license CC BY 4.0: <https://doi.org/10.6084/m9.figshare.26789641.v1>.

Code availability

Codes used for calculation and plotting in this manuscript are provided in https://github.com/YiYao1995/Yao_et_al_2024_IRRMIP_first_results.git⁷⁰.

References

- Döll, P., Fiedler, K. & Zhang, J. Global-scale analysis of river flow alterations due to water withdrawals and reservoirs. *Hydrol. Earth Syst. Sci.* **13**, 2413–2432 (2009).
- Tatsumi, K. & Yamashiki, Y. Effect of irrigation water withdrawals on water and energy balance in the Mekong River Basin using an improved VIC land surface model with fewer calibration parameters. *Agric. Water Manag.* **159**, 92–106 (2015).
- Zhu, B. & Huang, M. et al. Effects of irrigation on water, carbon, and nitrogen budgets in a semiarid watershed in the Pacific northwest: A modeling study. *J. Adv. Model. Earth Syst.* **12**, e2019MS001953 (2020).
- Al-Yaari, A., Ducharne, A., Thiery, W., Cheruy, F. & Lawrence, D. The role of irrigation expansion on historical climate change: insights from CMIP6. *Earth's Future* **10**, e2022EF002859 (2022).
- McDermid, S. et al. Irrigation in the Earth system. *Nat. Rev. Earth Env.* **4**, 435–453 (2023).
- Puma, M. & Cook, B. Effects of irrigation on global climate during the 20th century. *J. Geophys. Res.* **115**, D16120 (2010).
- Cook, B., Shukla, S., Puma, M. & Nazarenko, L. Irrigation as an historical climate forcing. *Clim. Dyn.* **44**, 1715–1730 (2015).
- Kang, S. & Eltahir, E. Impact of irrigation on regional climate over Eastern China. *Geophys. Res. Lett.* **46**, 5499–5505 (2019).
- Sacks, W., Cook, B., Buening, N., Levis, S. & Helkowski, J. Effects of global irrigation on the near-surface climate. *Clim. Dyn.* **33**, 159–175 (2009).
- Thiery, W. et al. Present-day irrigation mitigates heat extremes. *J. Geophys. Res.* **122**, 1403–1422 (2017).
- Huang, X. & Ullrich, P. Irrigation impacts on California's climate with the variable-resolution CESM. *J. Adv. Model. Earth Syst.* **8**, 1151–1163 (2016).
- Thiery, W. et al. Warming of hot extremes alleviated by expanding irrigation. *Nat. Commun.* **11**, 290 (2020).
- Hirsch, A., Wilhelm, M., Davin, E., Thiery, W. & Seneviratne, S. Can climate-effective land management reduce regional warming? *J. Geophys. Res.* **122**, 2269–2288 (2017).
- Kala, J., Valmassoi, A. & Hirsch, A. Assessing the maximum potential cooling benefits of irrigation in Australia during the “Angry Summer” of 2012/2013. *Weather Clim. Extremes* **39**, 100538 (2023).
- Cramer, M. & Jay, O. Biophysical aspects of human thermoregulation during heat stress. *Auton. Neurosci.* **196**, 3–13 (2016).
- Buzan, J. & Huber, M. Moist heat stress on a hotter Earth. *Annu. Rev. Earth Planet. Sci.* **48**, 623–655 (2020).
- Givoni, B. & Belding, H. The cooling efficiency of sweat evaporation, in *Biometeorology*, Elsevier. 304–314 (1962).
- Sorooshian, S., Li, J., Hsu, K. & Gao, X. How significant is the impact of irrigation on the local hydroclimate in California's Central Valley? Comparison of model results with ground and remote-sensing data. *J. Geophys. Res.* **116**, D06102 (2011).
- Lee, E., Sacks, W., Chase, T. & Foley, J. Simulated impacts of irrigation on the atmospheric circulation over Asia. *J. Geophys. Res.* **116**, D08114 (2011).
- Buzan, J., Oleson, K. & Huber, M. Implementation and comparison of a suite of heat stress metrics within the Community Land Model version 4.5. *Geosci. Model Dev.* **8**, 151–170 (2015).
- Zhao, Y., Ducharne, A., Sultan, B., Braconnot, P. & Vautard, R. Estimating heat stress from climate-based indicators: present-day biases and future spreads in the CMIP5 global climate model ensemble. *Environ. Res. Lett.* **10**, 084013 (2015).
- Mishra, V. et al. Moist heat stress extremes in India enhanced by irrigation. *Nat. Geosci.* **13**, 722–728 (2020).
- Krakauer, N., Cook, B. & Puma, M. Effect of irrigation on humid heat extremes. *Environ. Res. Lett.* **15**, 094010 (2020).
- Gates, W. et al. An overview of the results of the Atmospheric Model Intercomparison Project (AMIP I). *Bull. Am. Meteorol. Soc.* **80**, 29–56 (1999).
- Li, J., Han, Z. & Xie, Z. Model analysis of long-term trends of aerosol concentrations and direct radiative forcings over East Asia. *Tellus B* **65**, 20410 (2013).
- Babu, S. et al. Trends in aerosol optical depth over Indian region: potential causes and impact indicators. *J. Geophys. Res.* **118**, 11–794 (2013).
- Zhan, X., Kustas, W. & Humes, K. An intercomparison study on models of sensible heat flux over partial canopy surfaces with remotely sensed surface temperature. *Remote Sens. Environ.* **58**, 242–256 (1996).
- Yao, Y. et al. *Implementation and Evaluation of Irrigation Techniques in the Community Land Model*. (Verlag nicht ermittelbar, Fort Collins, Colo., 2022).
- De Hertog, S. et al. The biogeophysical effects of idealized land cover and land management changes in Earth system models. *Earth Syst. Dyn.* **14**, 629–667 (2023).
- Ambika, A. & Mishra, V. Improved water savings and reduction in moist heat stress caused by efficient irrigation. *Earth's Future* **10**, e2021EF002642 (2022).
- Alexandratos, N. & Bruinsma, J. World agriculture towards 2030/2050: the 2012 revision. (2012).
- Leng, G., Huang, M., Tang, Q. & Leung, L. A modeling study of irrigation effects on global surface water and groundwater resources under a changing climate. *J. Adv. Model. Earth Syst.* **7**, 1285–1304 (2015).
- Zhou, T. et al. Global irrigation characteristics and effects simulated by fully coupled land surface, river, and water management models in E3SM. *J. Adv. Model. Earth Syst.* **12**, e2020MS002069 (2020).
- Wisser, D., Fekete, B., Vörösmarty, C. & Schumann, A. Reconstructing 20th century global hydrography: a contribution to the Global Terrestrial Network-Hydrology (GTN-H). *Hydrol. Earth Syst. Sci.* **14**, 1–24 (2010).
- Decharme, B., Costantini, M., Colin, J. A simple approach to represent irrigation water withdrawals in Earth system models. *J. Adv. Model. Earth Syst.* (Under review, 2024).
- Arboleda-Obando, P. F., Ducharne, A., Yin, Z. & Ciais, P. Validation of a new global irrigation scheme in the land surface model ORCHIDEE v2. 2. *Geosci. Model Dev.* **17**, 2141–2164 (2024).
- Li, Y. et al. Quantifying irrigation cooling benefits to maize yield in the US Midwest. *Glob. Change Biol.* **26**, 3065–3078 (2020).
- Kang, S. & Eltahir, E. North China Plain threatened by deadly heatwaves due to climate change and irrigation. *Nat. Commun.* **9**, 2894 (2018).
- Jha, R., Mondal, A., Devanand, A., Roxy, M. & Ghosh, S. Limited influence of irrigation on pre-monsoon heat stress in the Indo-Gangetic Plain. *Nat. Commun.* **13**, 4275 (2022).
- Kukul, M. Comment on “Improved Water Savings and Reduction in Moist Heat Stress Caused by Efficient Irrigation” by Anukesh Krishnankutty Ambika and Vimal Mishra. *Earth's Future* **11**, e2022EF002892 (2023).
- Guo, Q., Zhou, X., Satoh, Y. & Oki, T. Irrigated cropland expansion exacerbates the urban moist heat stress in northern India. *Environ. Res. Lett.* **17**, 054013 (2022).
- Orlov, A. et al. Changes in land cover and management affect heat stress and labor capacity. *Earth's Future* **11**, e2022EF002909 (2023).
- De Hertog, S. et al. Limited effect of future land-use changes on human heat stress and labor capacity. *Earth's Future* **13**, e2024EF005021 (2025).
- Lo, Y. et al. Optimal heat stress metric for modelling heat-related mortality varies from country to country. *Int. J. Climatol.* **43**, 5553 (2023).
- Guo, Q. et al. Regional variation in the role of humidity on city-level heat-related mortality. *PNAS Nexus* **3**, pgae290 (2024).
- Vecellio, D., Kong, Q., Kenney, W. & Huber, M. Greatly enhanced risk to humans as a consequence of empirically determined lower moist

- heat stress tolerance. *Proc. Natl Acad. Sci. USA* **120**, e2305427120 (2023).
47. Williams, I. N., Pierrehumbert, R. T. & Huber, M. Global warming, convective threshold and false thermostats. *Geophys. Res. Lett.* **21**, L21805 (2009).
 48. Williams, I. & Pierrehumbert, R. Observational evidence against strongly stabilizing tropical cloud feedbacks. *Geophys. Res. Lett.* **44**, 1503–1510 (2017).
 49. Danabasoglu, G. et al. The community earth system model version 2 (CESM2). *J. Adv. Model. Earth Syst.* **12**, e2019MS001916 (2020).
 50. Felfelani, F., Lawrence, D. & Pokhrel, Y. Representing intercell lateral groundwater flow and aquifer pumping in the community land model. *Water Resources Research*. **57**, e2020WR027531 (2021).
 51. Boucher, O. et al. Presentation and evaluation of the IPSL-CM6A-LR climate model. *J. Adv. Model. Earth Syst.* **12**, e2019MS002010 (2020).
 52. Seland, Ø. et al. Overview of the Norwegian Earth System Model (NorESM2) and key climate response of CMIP6 DECK, historical, and scenario simulations. *Geosci. Model Dev.* **13**, 6165–6200 (2020).
 53. Golaz, J. C. et al. The DOE E3SM Model Version 2: overview of the physical model and initial model evaluation. *J. Adv. Model. Earth Syst.* **14**, e2022MS003156 (2022).
 54. Voltaire, A. et al. Evaluation of CMIP6 deck experiments with CNRM-CM6-1. *J. Adv. Model. Earth Syst.* **11**, 2177–2213 (2019).
 55. Colin, J., Decharme, B., Cattiaux, J. & Saint-Martin, D. Groundwater feedbacks on climate change in the CNRM global climate model. *J. Clim.* **36**, 7599–7617 (2023).
 56. Eyring, V. et al. Overview of the Coupled Model Intercomparison Project Phase 6 (CMIP6) experimental design and organization. *Geosci. Model Dev.* **9**, 1937–1958 (2016).
 57. Hurtt, G. et al. Harmonization of global land use change and management for the period 850–2100 (LUH2) for CMIP6. *Geosci. Model Dev.* **13**, 5425–5464 (2020).
 58. Klein Goldewijk, K., Beusen, A., Doelman, J. & Stehfest, E. Anthropogenic land use estimates for the Holocene-HYDE 3.2. *Earth Syst. Sci. Data* **9**, 927–953 (2017).
 59. Siebert, S. et al. A global data set of the extent of irrigated land from 1900 to 2005. *Hydrol. Earth Syst. Sci.* **19**, 1521–1545 (2015).
 60. Food and agriculture data. <https://www.fao.org/faostat/en/#home> (2024).
 61. Dahl, K., Licker, R., Abatzoglou, J. & Delet-Barreto, J. Increased frequency of and population exposure to extreme heat index days in the United States during the 21st century. *Environ. Res. Commun.* **1**, 075002 (2019).
 62. Masterton, J. & Richardson, F. *Humidex: A Method of Quantifying Human Discomfort Due to Excessive Heat and Humidity*. (Environment Canada, Atmospheric Environment, 1979)
 63. CCOHS Humidex Rating and Work. https://www.ccohs.ca/oshanswers/phys_agents/humidex.html (2023).
 64. Haldane, J. The influence of high air temperatures No. 1. *Epidemiol. Infect.* **5**, 494–513 (1905).
 65. Gupton Jr, W. *HVAC Controls: Operation and Maintenance*. (CRC Press, 2001)
 66. Stull, R. Wet-bulb temperature from relative humidity and air temperature. *J. Appl. Meteorol. Climatol.* **50**, 2267–2269 (2011).
 67. Sherwood, S. & Huber, M. An adaptability limit to climate change due to heat stress. *Proc. Natl Acad. Sci. USA* **107**, 9552–9555 (2010).
 68. Raymond, C., Matthews, T. & Horton, R. The emergence of heat and humidity too severe for human tolerance. *Sci. Adv.* **6**, eaaw1838 (2020).
 69. Yao, Y., Thiery, W. & Sterl, S. Winter is leaving: Reduced occurrence of extremely cold days in Belgium and implications for power system planning. (2020).
 70. Yao, Y. Codes for Impacts of irrigation expansion on moist-heat stress: first results from IRRMIP. *Zenodo* <https://doi.org/10.5281/zenodo.14626594> (2025).
 71. Iturbide, M. et al. An update of IPCC climate reference regions for subcontinental analysis of climate model data: definition and aggregated datasets. *Earth Syst. Sci. Data* **12**, 2959–2970 (2020).
 72. Savitzky, A. & Golay, M. Smoothing and differentiation of data by simplified least squares procedures. *Anal. Chem.* **36**, 1627–1639 (1964).

Acknowledgements

Y.Y. holds a China Scholarship Council (CSC) Studentship with Vrije Universiteit Brussel. W.T. acknowledges funding from the European Research Council (ERC) under the European Union's Horizon Framework research and innovation programme (grant agreement No. 101076909; 'LACRIMA' project). The computational resources and services used in this work for the storage and analysis of IRRMIP data were provided by the VSC (Flemish Supercomputer Center), funded by the Research Foundation—Flanders (FWO) and the Flemish Government—department EWI. The computational resources used for CESM2 simulations are supported by the CESM Land Model Working Group from the National Center of Atmosphere Research (NCAR; Project # P93300641). A.D. and P.-F. A.-O. got support from the Belmont Forum (project BLUEGEM, grant No. ANR-21-SOIL-0001), and their simulations were done using the IDRIS computational facilities (Institut du Développement et des Ressources en Informatique Scientifique, CNRS, France), S.D.H. acknowledges funding by BELSPO (B2/223/P1/DAMOCO). L.R.L. and T.Z. are supported by Office of Science, U.S. Department of Energy (DOE) Biological and Environmental Research through the Water Cycle and Climate Extremes Modeling (WACCEM) scientific focus area funded by the Regional and Global Model Analysis program area for performing the simulations and analyses, and the E3SM project through the Earth System Model Development program area for performing the model development. Pacific Northwest National Laboratory is operated for DOE by Battelle Memorial Institute under contract DE-AC05-76RL01830. NorESM simulations were performed using Computational Resources from the NN8057K project provided by Sigma2— the National Infrastructure for High-Performance Computing and Data Storage in Norway. Y.P. received support from the National Science Foundation (Belmont Forum project BLUEGEM; Award #: 2127643).

Author contributions

Y.Y. and W.T. designed the study and coordinated IRRMIP. Y.Y. wrote the manuscript with support from all authors and performed all analyses under the supervision of W.T. Y. Y., A. D., B. I. C., K. S. A., D. M. L., Y. P., P. L., L. R. L., J. J., J. C., B. D., S. M., N. H., Y. S., T. Y. and X. W. participated in the protocol design of IRRMIP. The IRRMIP simulations were performed by Y. Y., S. D. H., P. L., D. M. L., W. R. W. for the CESM2 model, by R. W., M. L., and Y. P. for the CESM2_gw model, by D. N. and K. S. A. for the NorESM model, by T. Z., L. R. L. for the E3SM model, by P.-F. A.-O. and A. D. for IPSL-CM6 model, by J. C., M. C. and B. D. for CNRM-CM6-1 model. J. B. provided guidance on the calculation of heat metrics. P. M., P. A. O., J. C., D. N., R. W., T. Z., M. E., L. S. N., M. C., K. O., Y. S. and L. J. supported the data transfer, data standardisation, and data storage for IRRMIP. V. M. and S. G. provided valuable insights and comments on the discussion regarding irrigation-induced impacts over specific regions.

Competing interests

The authors declare no competing interests.

Additional information

Supplementary information The online version contains supplementary material available at <https://doi.org/10.1038/s41467-025-56356-1>.

Correspondence and requests for materials should be addressed to Yi Yao.

Peer review information *Nature Communications* thanks Qiang Guo and the other, anonymous, reviewer for their contribution to the peer review of this work. A peer review file is available.

Reprints and permissions information is available at <http://www.nature.com/reprints>

Publisher's note Springer Nature remains neutral with regard to jurisdictional claims in published maps and institutional affiliations.

Open Access This article is licensed under a Creative Commons Attribution-NonCommercial-NoDerivatives 4.0 International License, which permits any non-commercial use, sharing, distribution and reproduction in any medium or format, as long as you give appropriate credit to the original author(s) and the source, provide a link to the Creative Commons licence, and indicate if you modified the licensed material. You do not have permission under this licence to share adapted material derived from this article or parts of it. The images or other third party material in this article are included in the article's Creative Commons licence, unless indicated otherwise in a credit line to the material. If material is not included in the article's Creative Commons licence and your intended use is not permitted by statutory regulation or exceeds the permitted use, you will need to obtain permission directly from the copyright holder. To view a copy of this licence, visit <http://creativecommons.org/licenses/by-nc-nd/4.0/>.

© The Author(s) 2025

¹Department of Water and Climate, Vrije Universiteit Brussel, Brussels, Belgium. ²Laboratory 7619 METIS, Sorbonne Université, CNRS, EPHE, IPSL, Paris, France. ³Department of Environmental Studies, New York University, New York, NY, USA. ⁴Q-ForestLab, Department of Environment, Universiteit Gent, Ghent, Belgium. ⁵CICERO - Center for International Climate Research, Oslo, Norway. ⁶Climate and Environmental Physics, Physics Institute, University of Bern, Bern, Switzerland. ⁷Oeschger Centre for Climate Change Research, University of Bern, Bern, Switzerland. ⁸Centre National de Recherches Météorologiques (CNRM), Université de Toulouse, Météo-France, Toulouse, France. ⁹Climate and Global Dynamics Laboratory, National Center for Atmospheric Research, Boulder, USA. ¹⁰Atmospheric, Climate, and Earth Sciences Division, Pacific Northwest National Laboratory, Richland, WA, USA. ¹¹Department of Atmospheric Sciences, National Taiwan University, Taipei, Taiwan. ¹²Advanced Computing Facility Unit, CSC- IT Center for Science, Espoo, Finland. ¹³Columbia University, Climate School, New York, NY 10025, USA. ¹⁴NASA Goddard Institute for Space Studies, New York, NY 10025, USA. ¹⁵Potsdam Institute for Climate Impact Research (PIK), Member of the Leibniz Association, 14412 Potsdam, Germany. ¹⁶Department of Civil and Environmental Engineering, Michigan State University, East Lansing, MI, USA. ¹⁷National Institute for Environmental Studies, Tsukuba 305-8506, Japan. ¹⁸Moon Soul Graduate School of Future Strategy, Korea Advanced Institute of Science and Technology, Daejeon, Republic of Korea. ¹⁹Sino-French Institute for Earth System Science, College of Urban and Environmental Sciences, Peking University, Beijing, China. ²⁰Civil Engineering, Indian Institute of Technology (IIT), Gandhinagar, India. ²¹Earth Sciences, Indian Institute of Technology (IIT), Gandhinagar, India. ²²Interdisciplinary Program in Climate Studies, Indian Institute of Technology Bombay, Mumbai, India.

✉ e-mail: yi.yao@vub.be